SUPPORTING INFORMATION

Exploring the intra-4f and the bright white light upconversion emissions of Gd_2O_3: Yb^{3+}, Er^{3+} based materials for thermometry

Talita J. S. Ramos[1,2], Ricardo L. Longo[1*], Carlos D. S. Brites[2], Rute A. S. Ferreira[2], Oscar L. Malta[1], and Luís D. Carlos[2*]

[1] Departamento de Química Fundamental. Universidade Federal de Pernambuco, 50740-540, Recife, PE, Brazil.

[2]Phantom-g, CICECO – Aveiro Institute of Materials, Department of Physics, University of Aveiro, 3810-193 Aveiro, Portugal.

*E-mail: ricardo.longo@ufpe.br; lcarlos@ua.pt

Contents

1. Structural characterization

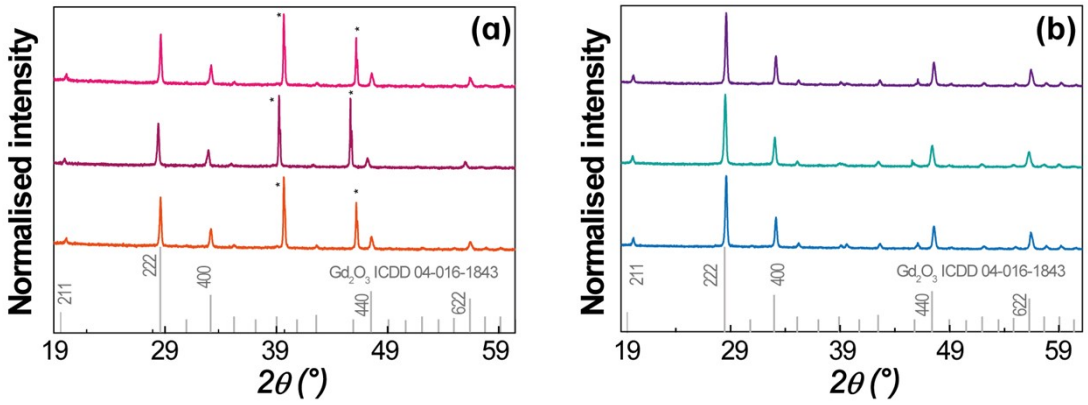

Fig. S1. X-ray powder diffraction patterns of **1** under (a) heating and (b) heating/vacuum cycles. In (a), the lines in orange, violet, and pink correspond to ambient temperature, 1273 K, and ambient temperature after the heating cycle. In **(b)**, the lines in blue, dark-cyan, and violet corresponds to ambient conditions, 1273 K in vacuum at 10^{-5} bar, and ambient conditions after the heating/pressure cycle. The reflections of cubic Gd_2O_3 are also depicted. The asterisks denote the Pt wire attached to the sample holder used to raise the temperature.

Representative scanning transmission electron microscope (STEM) images of **1** and **2** are shown in **Fig. S2**a,b. In **1** the average size of the agglomerates is smaller, as expected due to the nanosized nature of the system and in accord with the crystallite size estimated by XRD (Scherrer equation). EDS analysis of the two samples reports peaks attributed to Gd, Yb, and Er elements, as expected. The lower amount of Yb and Er and the spectral overlap with Al peaks precludes an accurate quantification of their relative amounts.

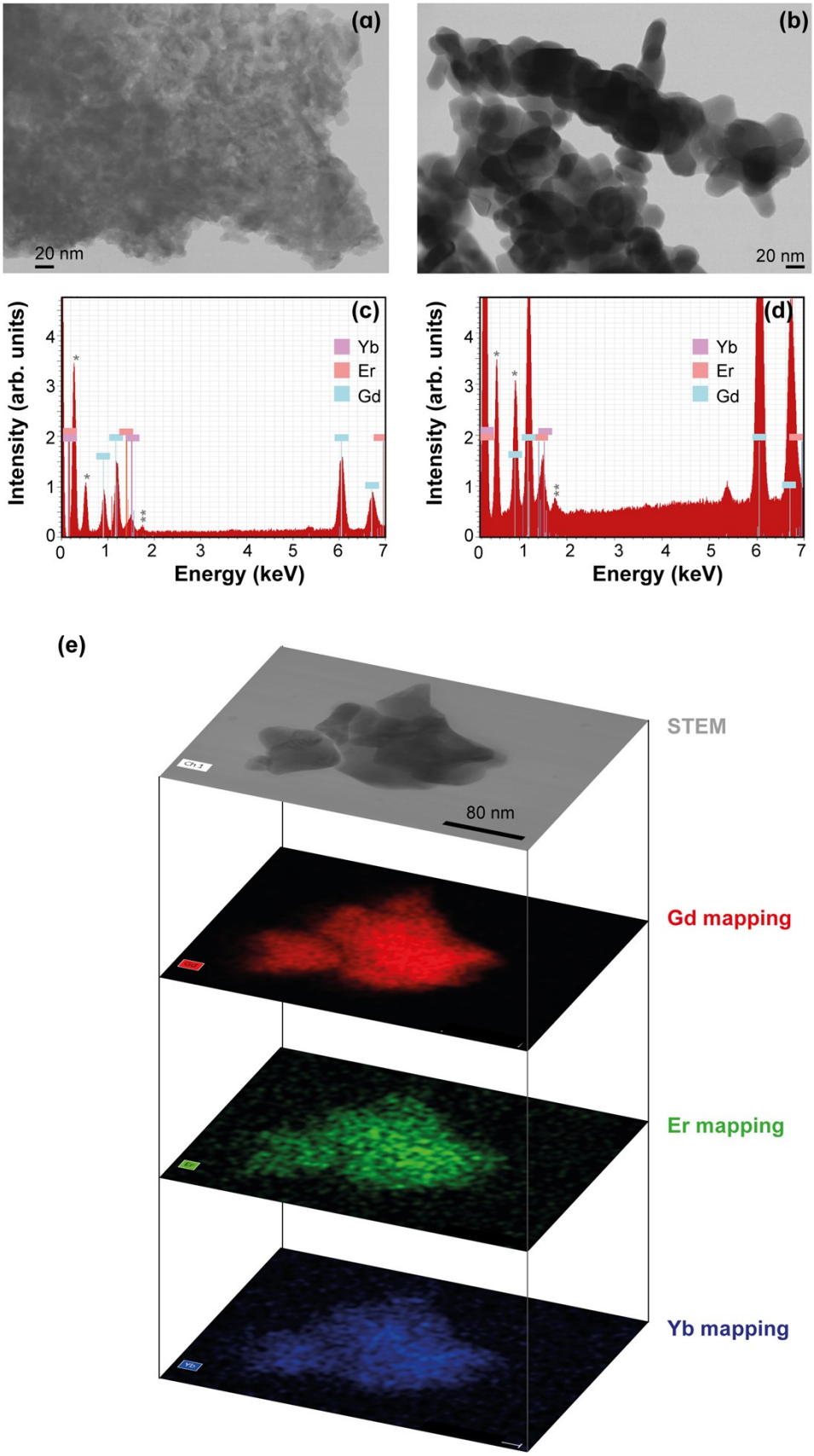

Figure S2. STEM images of **(a) 1** and **(b) 2** and corresponding EDS profiles, **(c)** and **(d)**, respectively. The peaks marked with asterisks denote the Cu (*) and Al (**) elements arising from the grids and the sample holder, respectively. **(e)** Illustrative STEM image of 2 and corresponding Gd, Er, and Yb elemental distributions.

Table S1. Values of the slopes n resulting from the best fit (in a log-log plot) to $\log(I_{UC}) \propto n \times \log(P_D)$, where I_{UC} is the integrated intensity of the corresponding transition and P_D the laser power density ($W \cdot cm^{-2}$), for **1** and **2**. The values of pressure (p, bar) and temperature (T, K) at which the emission spectra were recorded are indicated.

Sample		$^4H_{11/2} \rightarrow {}^4I_{15/2}$	$^4S_{3/2} \rightarrow {}^4I_{15/2}$	$^4F_{9/2} \rightarrow {}^4I_{15/2}$	p (bar)	T (K)
1	powder	0.9 ± 0.1	0.5 ± 0.1	0.7 ± 0.1	ambient	297
2	powder	1.1 ± 0.1	0.8 ± 0.1	0.8 ± 0.1	ambient	297
1	pellet	1.5 ± 0.3	1.9 ± 0.2	1.7 ± 0.3	ambient	297
1	pellet	1.6 ± 0.1	0.9 ± 0.1	0.7 ± 0.1	ambient	314
1	pellet	1.2 ± 0.2	0.5 ± 0.1	0.3 ± 0.1	7×10^{-5}	309
1	pellet	1.4 ± 0.2	0.7 ± 0.1	0.5 ± 0.1	2×10^{-5}	306

2. Energy gap determination

The energy gap (ΔE) between the $^2H_{11/2}$ and $^4S_{3/2}$ levels was determined based on the barycenter of the $^2H_{11/2} \rightarrow {}^4I_{15/2}$ and $^4S_{3/2} \rightarrow {}^4I_{15/2}$ transitions in the emission spectrum of the samples when irradiated upon 980 nm at 16.4 $W \cdot cm^{-2}$. The region corresponding to the $^2H_{11/2} \rightarrow {}^4I_{15/2}$ (I_H) and $^4S_{3/2} \rightarrow {}^4I_{15/2}$ (I_S) transitions were fitted using Gaussian functions by peak analyzer routine of the OriginLab© software (Figure S3). The barycenters of the $^2H_{11/2}$ and $^4S_{3/2}$ levels are calculated by weighted the arithmetic mean using the fitted area, A_i, and peak energy, v_i, of each, i, Gaussian function, Eq. S1. The energy gap (ΔE) results from the difference between the barycenters of the two transitions:

$$E_{H,S} = \frac{v_1 A_1 + \ldots + v_n A_n}{A_1 + \ldots + A_n} \quad \textbf{(S1)}$$

The corresponding error ($\delta \Delta E$) was determined by:

$$\delta \Delta E = \sqrt{\delta E_H^2 + \delta E_S^2} \quad \textbf{(S2)}$$

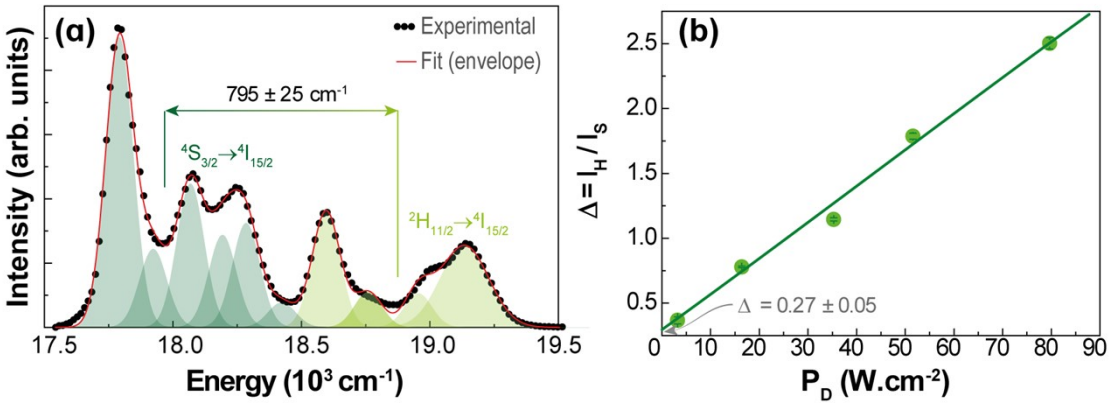

Figure S3. (a) Spectral Gaussian deconvolution of the emission spectrum of **1** measured at 297 K and 16.4 W·cm^{-2}. The black dots and the red line represent the experimental data and the fit envelope of the spectrum, respectively. The shadowed areas correspond to the Gaussian functions assigned to the $^2H_{11/2}\rightarrow{}^4I_{15/2}$ (light green) and $^4S_{3/2}\rightarrow{}^4I_{15/2}$ (dark green) transitions. **(b)** Dependence on the pump power laser density of the thermometric parameter (Δ) for **1** (in pellet, at ambient conditions). The error bar represents the uncertainty in Δ. The line represents the fit to the experimental data using a straight line (r^2>0.995). In the limit of the lowest P_D value, the sample temperature (T_0 = 297.1 K) corresponds to the room temperature, *i.e.,* to the absence of laser-induced heating.

3. Thermometric analysis

The uncertainty of the thermometric parameter, Eq. S3 is estimated using the signal-to-noise values, typically calculated dividing the readout fluctuations of the baseline by the maximum intensity value of the $^2H_{11/2}\rightarrow{}^4I_{15/2}$ (I_H) and $^4S_{3/2}\rightarrow{}^4I_{15/2}$ (I_S) transitions. The readout fluctuation is estimated by the standard deviation of points in the baseline between 17537 and 17214 cm^{-1}:

$$\frac{\delta\Delta}{\Delta}=\sqrt{\left(\frac{\delta I_H}{I_H}\right)^2+\left(\frac{\delta I_S}{I_S}\right)^2} \qquad \textbf{(S3)}$$

Relative thermal sensitivity

The relative thermal sensitivity (S_r) is defined as:

$$S_r=\frac{1}{\Delta}\left|\frac{\partial\Delta}{\partial T}\right|=\frac{\Delta E}{k_B T^2} \qquad \textbf{(S4)}$$

where the last equality is valid for thermometric parameter with the following equation: $\Delta = Ae^{-\Delta E/(k_B T)}$, with A being a constant (independent of the temperature), ΔE is the energy

gap between the thermally-coupled levels, k_B is the Boltzmann constant, and T is the temperature.

The error related to the relative thermal sensitivity (δS_r, Eq. S5) was derived from the errors of the parameters used in the calculation of S_r (Eq. S4), where $\delta\Delta E$ is the error in ΔE and $\theta T = 0.1$ K is the uncertainty in the temperature measured by the thermocouple.

$$\delta S_r = S_r \sqrt{\left(\frac{\delta \Delta E}{\Delta E}\right)^2 + \left(-2\frac{\theta T}{T}\right)^2} \quad \textbf{(S5)}$$

The temperature uncertainty is:

$$\delta T = \frac{1}{S_r}\frac{\delta \Delta}{\Delta} \quad \textbf{(S6)}$$

The error in the temperature calculated by Eq. 1 (main manuscript), σ_T, is given by:

$$\sigma_T = T^2 \sqrt{\left(\frac{\delta T_0}{T_0^2}\right)^2 + \left(\frac{k_B}{\Delta E}\right)^2 \left[\left(\frac{\delta \Delta E}{k_B} \ln\left(\frac{\Delta}{\Delta_0}\right)\right)^2 + \left(\frac{\delta \Delta}{\Delta}\right)^2 + \left(\frac{\delta \Delta_0}{\Delta_0}\right)^2\right]}. \quad \textbf{(S7)}$$

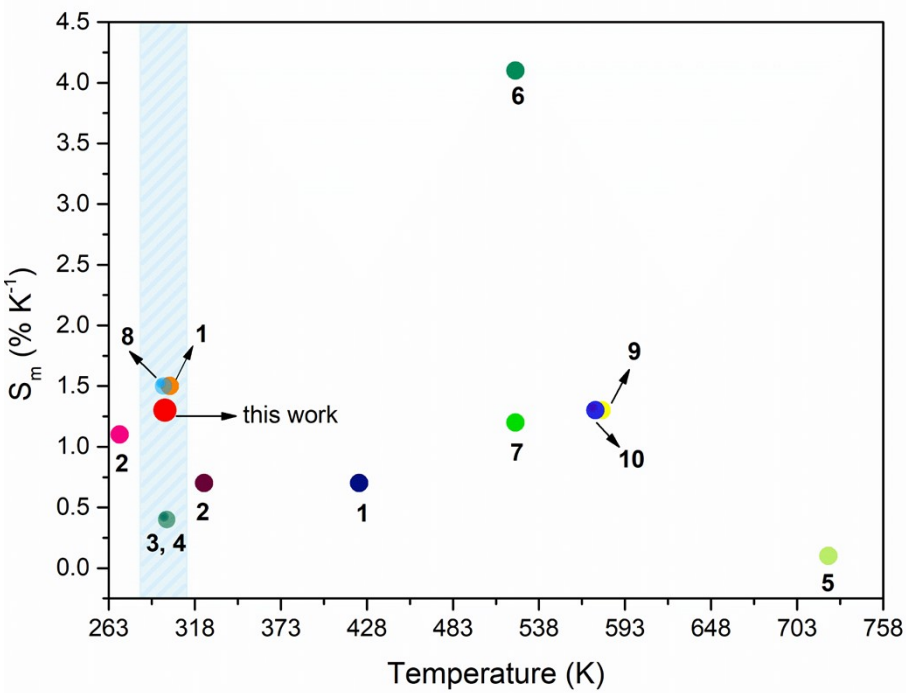

Figure S4. Temperature dependence of the maximum relative thermal sensitivity (S_m) of some Gd_2O_3:Yb^{3+}, Er^{3+} reported in the literature, Table S2. The blue area represents the physiological temperature range.

Table S2. Comparison of temperature sensing parameters, operating range (ΔT), laser power (P) or laser power density (P_D), maximum relative sensitivity (S_m), corresponding maximum temperature (T_m), and temperature uncertainty (δT), of Gd_2O_3: Yb^{3+}, Er^{3+} samples under excitation at or near 980 nm. The thermometric performance was determined by the fluorescence intensity ratio (FIR) methodology.

Phosphor	ΔT (K)	P (10^{-3} W)	P_D (W·cm^{-2})	S_m (% K^{-1})	T_m (K)	δT (K)	Ref.
$(Gd_{0.89}Yb_{0.10}Er_{0.01})_2O_3$ (**1**)	299–363		16	1.3	299	0.1	This work
Gd_2O_3:(3%)Yb^{3+}/(2%)Er^{3+}-AuNPs-1.25%	301–615		32–600	1.5	302	1.0	[1]
Gd_2O_3:(3%)Yb^{3+}/(2%)Er^{3+}-AuNPs-2.50%	423–1050		95–455	0.7	423	2.0	[1]
Gd_2O_3:(2%)Yb^{3+}/(1%)Er^{3+}	270–357		42–488	1.1	270		[2]
Gd_2O_3:(10%)Yb^{3+}/(1%)Er^{3+}	324–612		42–488	0.7	324		[2]
(100−x−y)Gd_2O_3:x%Yb_2O_3+y% Er_2O_3, x: 0.0-0.6% and y: 0.0-3.5%	300–900	0-28		0.4	300		[3]
(100−x−y) Gd_2O_3+xYb_2O+yEr_2O_3, x: 0.0 to 0.6 % and y: 0.0 to 3.5 %	300–900	2–6		0.4	300		[4]
Gd_2O_3:(5 %) Yb^{3+}/ (2 %) Er^{3+}	298–723		1–4	0.1	723		[5]
Gd_2O_3:(1%)Yb^{3+}/(1%)Er^{3+}	303–523	165 358*		4.1	523		[6]
Gd_2O_3:(4%)Yb^{3+}/(1%)Er^{3+}	300–523		0.8	1.2	523	2.7	[7]
Gd_2O_3:(6%)Yb^{3+}/(1%)Er^{3+}	324–612		0.8	1.2	523	3.3	[7]
Gd_2O_3:(10%)Yb^{3+}/(1%)Er^{3+}	298–578	10		1.5	298		[8]
Gd_2O_3:(10%)Yb^{3+}/(1%)Er^{3+}	298−578		2.8	1.3	578		[9]
Gd_2O_3:(7.0%)Yb^{3+}/(3.5%)Er^{3+}	300−575	3.0-7.0		1.3	574		[10]

*Co-excitation wavelength at 980 nm and 1550 nm.

4. White-light emission

4.1. Excitation wavelength

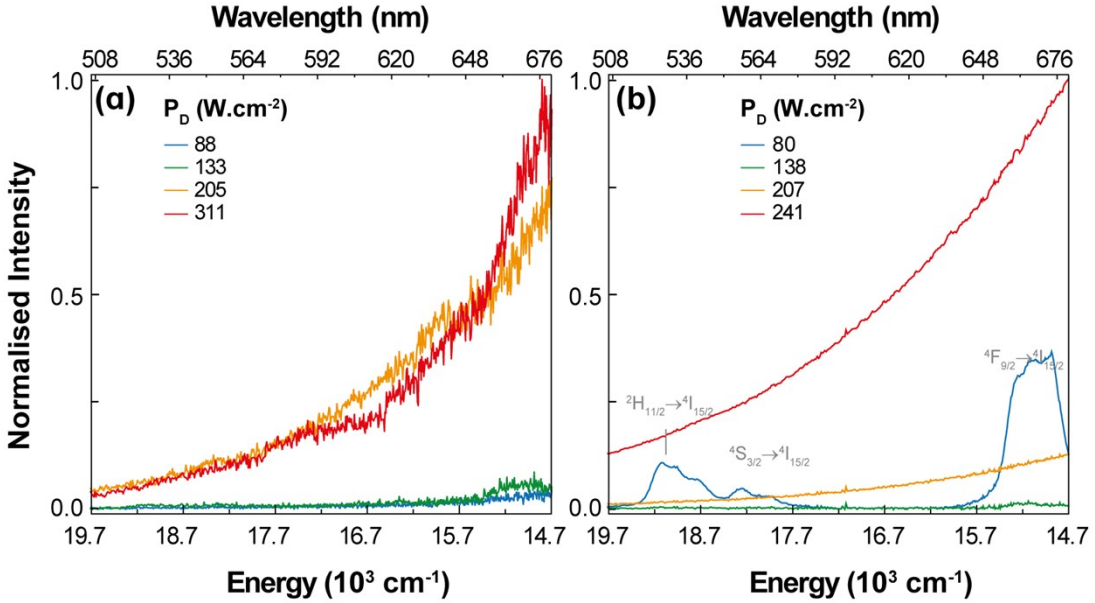

Figure S5. Upconversion emission spectra of **1**, in pellet and at ambient conditions, excited at **(a)** 808 nm and **(b)** 980 nm.

The emission spectra upon excitation at 980 nm and at 808 nm were obtained under different circumstances (days apart, different slits, and different acquisition times) and they cannot be directly compared. However, it can be inferred that the excitation at 980 nm leads to brighter white light emission compared to excitation at 808 nm with approximately the same excitation power density, because the signal-to-noise ratios are much higher for the spectra excited at 980 nm than at 808 nm, for which larger slits and longer acquisition times were employed. These observations are explained by the higher concentration of Yb^{3+} (10%) and its larger absorption cross section at 980 nm compared to the lower concentration of Er^{3+} (1%) and its smaller cross section at 808 nm in the sample, $(Gd_{0.89}Yb_{0.1}Er_{0.01})_2O_3$.

4.2. Pump power dependence and powder versus pellets

Table S3. Slopes of the dependence of the integrated intensity of white light emission, I_{WL}, with P_D (in a log-log plot) of **1** and **2** in powder and pellets at different pressures and room temperature.

Sample		Slope	r^2	*p* (bar)
1	powder	3.9 ±0.2	0.986	ambient pressure
2		3.8 ±0.5	0.955	
1	pellet	6.1 ±0.6	0.966	
		7.2 ±0.5	0.974	7×10^{-5}
		4.2 ±0.4	0.970	2×10^{-5}

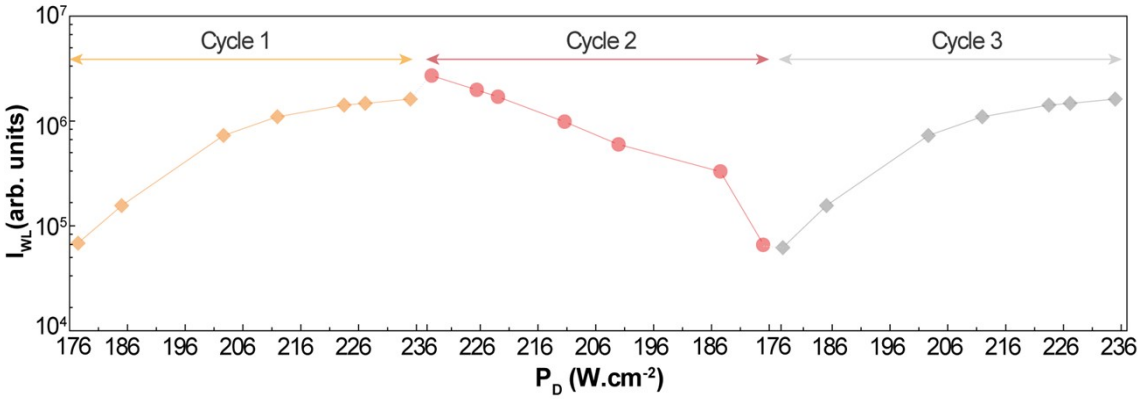

Figure S6. P_D dependence of the integrated intensity of the white light emission (I_{WL}) of **2** (powder) recorded in three cycles of irradiation. In cycles **1** (forward) and **2** (reverse), the powder was irradiated at the same spot, whereas in cycle 3 the measurement was performed on several points of the sample.

4.3. Pressure dependence

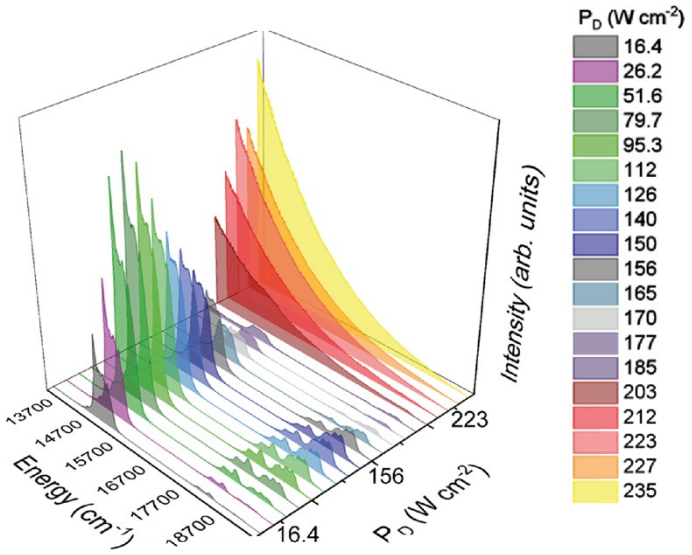

Figure S7. Emission spectra of **1** in pellet obtained at ambient conditions as a function of P_D.

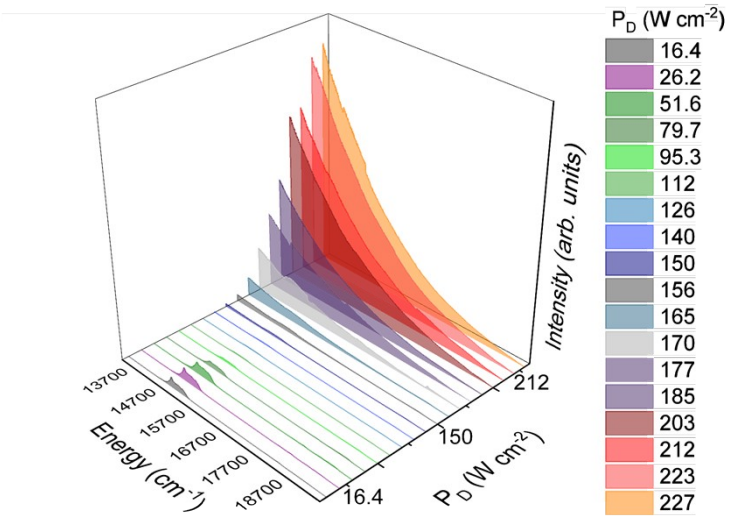

Figure S8. Emission spectra of **1** in pellets and at 7×10^{-5} bar as a function of P_D.

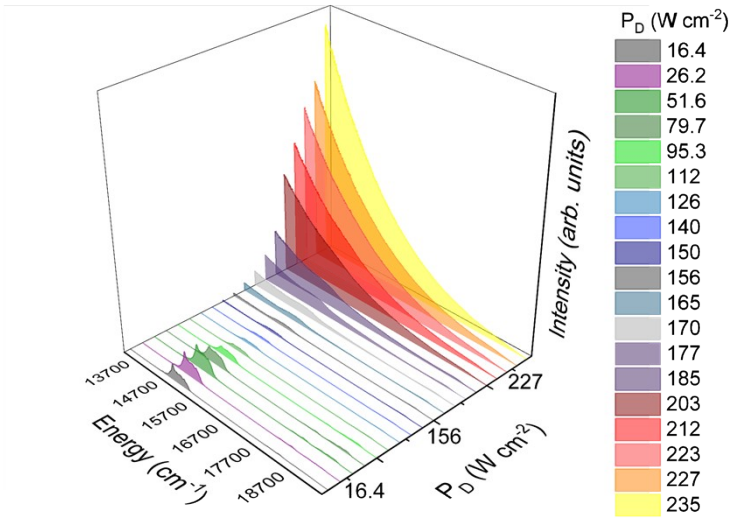

Figure S9. Emission spectra of **1** in pellets and at 2×10^{-5} bar as a function of P_D.

4.4. Temperature determination from Planck's Law

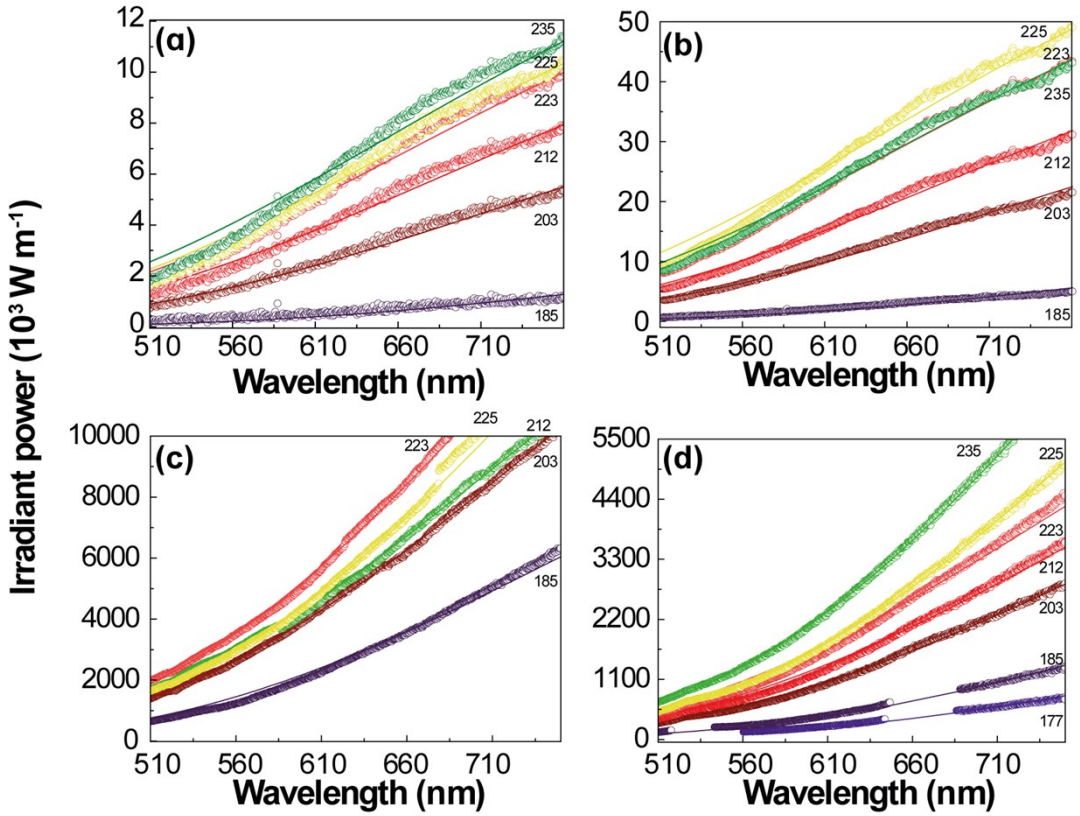

Figure S10. Fitting of the emission spectra acquired at different values of P_D for (a) **2** in powder at ambient pressure, (b) **1** in powder at ambient pressure, (c) **1** in pellet at 7×10^{-5} bar, and (d) **1** in pellet at 2×10^{-5} bar using Planck's law.

Table S4. Fitting results of the continuous upconversion emission spectra (Figure 5c in the main manuscript) to Eq. (2) with $A = 4.20\times10^{-21}$ and $T = 0.014388/B$ for **1** (pellet) under 980 nm excitation at ambient pressure. The fitted temperatures are represented in Fig. 5d in the main manuscript.

P_D (W·cm^{-2})	B ($\times10^{-6}$)	ΔB ($\times10^{-9}$)	R^2	T (K)
177	7.54	1.57	0.989	1907.8±0.4
185	7.15	8.98	0.997	2013.4±0.3
203	6.59	0.566	0.998	2183.1±0.2
212	6.43	0.902	0.995	2237.1±0.3
223	6.29	1.18	0.990	2288.9±0.4
225	6.22	1.68	0.981	2315.0±0.6
235	6.04	2.01	0.973	2382.5±0.8

Table S5. Same as Table S4 for **2** (powder) at ambient pressure (Figure S10a) and $A = 3.72\times10^{-24}$. The fitted temperatures are represented in Fig. 5d in the main manuscript.

P_D (W·cm^{-2})	B ($\times10^{-6}$)	ΔB ($\times10^{-9}$)	R^2	T (K)
185	7.06	5.47	0.822	2037±2
203	5.97	1.39	0.989	2411±1
212	5.69	1.41	0.988	2528±1
223	5.52	1.61	0.984	2607±1
225	5.49	1.66	0.983	2619±1
235	5.43	1.72	0.982	2648±1

Table S6. Same as Table S4 for **1** (powder) at ambient pressure (Figure S10b) and $A = 1.51\times10^{-23}$. The fitted temperatures are represented in Fig. 5d in the main manuscript.

P_D (W·cm^{-2})	B ($\times10^{-6}$)	ΔB ($\times10^{-9}$)	R^2	T (K)
185	6.48	1.17	0.951	2053.7±0.9
203	7.01	3.21	0.990	2412.9±0.5
212	5.96	1.30	0.991	2523.3±0.5
223	5.70	1.23	0.987	2631.4±0.7
225	5.47	1.42	0.985	2673.5±0.8

Table S7. Same as Table S4 for **1** (pellet) at 7×10^{-5} bar (Figure S10c) and $A = 7.08\times10^{-21}$. The fitted temperatures are represented in Fig. 5d in the main manuscript.

P_D (W·cm^{-2})	B ($\times10^{-6}$)	ΔB ($\times10^{-9}$)	R^2	T (K)
185	6.75	1.41	0.999	2130.6±0.4
203	6.17	1.13	0.688	2332.2±0.4
212	5.96	0.48	0.998	2413.3±0.2
223	5.81	1.35	0.985	2477.5±0.6

Table S8. Same as Table S4 for **1** (pellet) at 2×10^{-5} bar (Figure S10d) and $A = 4.42\times10^{-21}$. The fitted temperatures are represented in Fig. 5d in the main manuscript.

P_D (W·cm^{-2})	B ($\times10^{-6}$)	ΔB ($\times10^{-9}$)	R^2	T (K)
177	7.54	1.57	0.989	1907.8±0.4
185	7.15	8.98	0.997	2013.4±0.3
203	6.59	0.566	0.998	2183.1±0.2
212	6.43	0.902	0.995	2237.1±0.3
223	6.29	1.18	0.990	2288.9±0.4
225	6.22	1.68	0.981	2315.0±0.6
235	6.04	2.01	0.973	2382.5±0.8

Table S9. Slopes of the dependence of the calculated temperature, Eq. (2), with P_D of **1** and **2** in powder and pellets at different pressures, represented in Fig. 5d in the manuscript.

Sample		Slope	r^2	p (bar)
1	powder	10 ± 1	0.860	ambient pressure
2		13 ± 1	0.971	
1	pellet	6 ± 1	0.940	
		9 ± 1	0.966	7×10^{-5}
		8 ± 1	0.949	2×10^{-5}

5. Estimating the thermal conductivity

The effective thermal conductivity, $\langle k \rangle$, of a porous material can be approximated as[11]

$$\frac{\langle k \rangle}{k_f} = \left(\frac{k_s}{k_f}\right)^{0.28 - 0.757\log(\langle \varepsilon \rangle) - 0.057\log\left(k_s/k_f\right)}$$

where $\langle \varepsilon \rangle$ is the effective porosity, k_s is the thermal conductivity of the solid, and k_f is the thermal conductivity of the fluid. Thus, $\langle k \rangle$ decreases with increasing porosity $\langle \varepsilon \rangle$.

For Gd_2O_3, the thermal conductivity at room temperature was determined as being 1.72 to 3.15 $W\,m^{-1}\,K^{-1}$, depending on the time and the temperature of sintering,[12] as 4.3 $W\,m^{-1}\,K^{-1}$ for monoclinic Gd_2O_3 ceramics,[13] and as 3.2±0.5 $W\,m^{-1}\,K^{-1}$ for microwave sintered (at 1500 °C).[14]

At room temperature, considering $k_s \cong 2.6\ W\,m^{-1}\,K^{-1}$ for Gd_2O_3, and $k_f \cong 0.026\ W\,m^{-1}\,K^{-1}$ for air, the effective thermal conductivity becomes,

$$\langle k \rangle = 0.026 \times 100^{(0.166 - 0.757\log\langle \varepsilon \rangle)}$$

which for $\langle \varepsilon \rangle = 0.4$ gives $\langle k \rangle = 0.22\ W\,m^{-1}\,K^{-1}$ and for $\langle \varepsilon \rangle = 0.8$ gives $\langle k \rangle = 0.078\ W\,m^{-1}\,K^{-1}$. These values of the effective porosity represent consolidated (e.g., compact pellets) and unconsolidated nanopowders of similar material.[11, 15, 16]

The thermal conductivity of gases, k_p, at very low pressures (for Knudsen number larger than 1), can be approximated as[17]

$$\frac{k_p}{k_0} = \frac{1}{1 + C\bar{T}/pd}$$

where k_0 is the thermal conductivity of the gas at room pressure and temperature, C is a constant, which for air is $7.6 \times 10^{-5}\ N\,m^{-1}\,K^{-1}$, p (in Pa) is the pressure, d (in m) is the distance between the plates (or the distance between the two regions defining the temperature gradient), and $\bar{T}$ (in K) the average temperature of the plates (or the average temperature of the regions responsible for the temperature gradient).

For an average temperature of $\bar{T} \cong (1700 + 300)/2 =$ 1000 K, and $d = 0.76\ mm$, then

$$\frac{k_p}{k_0} \cong \frac{1}{1 + 100/p}$$

which gives a value of $k_p/k_0 = 0.0196$ for $p = 2\ Pa = 2 \times 10^{-5}\ bar$. Or, the thermal conductivity of air decreases ca. 50-fold from 1 bar to 2 Pa.

6. Experimental procedure to temporal analysis

The data acquisition procedure for the temporal analysis is the following:

1) Set laser (980 nm, ca. 102.6 W·cm^{-2}) and wait 30 minutes for stabilization (shutter closed).
2) Set parameters for spectral acquisition.
3) Start measurement.
4) Open the laser shutter at t = 15 s.
5) Close the laser shutter at t = 75 s.
6) End of measurement at t = 105 s.
7) Save data and check the transient curve.
8) Optimize parameters if needed.

9) Repeat steps 3-7 (4 times).

7. References

1. Debasu, M. L.; Ananias, D.; Pastoriza-Santos, I.; Liz-Marzán, L. M.; Rocha, J.; Carlos, L. D. All-in-One Optical Heater-Thermometer Nanoplatform Operative from 300 to 2000 K Based on Er^{3+} Emission and Blackbody Radiation. *Adv. Mater.* **2013,** *25* (35), 4868-4874.
2. Lei, Y.; Song, H.; Yang, L.; Yu, L.; Liu, Z.; Pan, G.; Bai, X.; Fan, L. Upconversion Luminescence, Intensity Saturation Effect, and Thermal Effect in Gd_2O_3: Er^{3+}, Yb^{3+} Nanowires. *J. Chem. Phys.* **2005,** *123* (17), 174710-174715.
3. Singh, S. K.; Kumar, K.; Rai, S. B. Er^{3+}/Yb^{3+} Codoped Gd_2O_3 Nano-Phosphor for Optical Thermometry. *Sens. Actuators A: Phys.* **2009,** *149* (1), 16-20.
4. Singh, S. K.; Kumar, K.; Rai, S. B. Multifunctional Er^{3+}-Yb^{3+} Codoped Gd_2O_3 Nanocrystalline Phosphor Synthesized through Optimized Combustion Route. *Appl. Phys. B-Lasers O* **2009,** *94* (1), 165-173.
5. Tian, Y.; Tian, B. N.; Cui, C. E.; Huang, P.; Wang, L.; Chen, B. J. Size-Dependent Upconversion Luminescence and Temperature Sensing Behavior of Spherical Gd_2O_3:Yb^{3+}/Er^{3+} Phosphor. *RSC Adv.* **2015,** *5* (19), 14123-14128.
6. Hao, H. Y.; Zhang, X. R.; Wang, Y. X.; Liang, L. Color Modulation and Temperature Sensing Investigation of Gd_2O_3: 1 Mol% Er^{3+}, 1 Mol% Yb^{3+} Phosphors under Different Excitation Condition. *J. Lumin.* **2019,** *215*, 116556.
7. Hao, H. Y.; Zhang, X. R.; Wang, Y. X.; Li, L. Up-Conversion Luminescence of Yb^{3+}/Er^{3+} Doped Gd_2O_3 Phosphors for Optical Temperature Sensing in Green and Red Regions. *Opt. Commun.* **2019,** *452*, 387-394.
8. Zheng, W.; Sun, B. Y.; Li, Y. M.; Lei, T. Y.; Wang, R.; Wu, J. Z. Low Power High Purity Red Upconversion Emission and Multiple Temperature Sensing Behaviors in Yb^{3+},Er^{3+} Codoped Gd_2O_3 Porous Nanorods. *ACS Sustain. Chem. Eng.* **2020,** *8* (25), 9578-9588.
9. Zheng, W.; Sun, B. Y.; Li, Y. M.; Wang, R. Gd_2O_3:Er^{3+},Yb^{3+} Upconversion Nanoparticle-Based Thermometry for Temperature Monitoring. *ACS Appl. Nano Mater.* **2021,** *4* (4), 3922-3931.
10. Li, Z. H.; Han, Q.; Yan, T. P.; Huang, Z. J.; Song, Y. L.; Wang, Y. X.; Zhang, X. R. Up-Conversion Luminescence and Optical Temperature Sensing of Er^{3+}, Yb^{3+} Co-Doped Gd_2O_3 Phosphors with Different F^-/Ln^{3+}. *J. Alloy. Compd.* **2022,** *904*, 164009.
11. M. Kaviany, Principles of Heat Transfer in Porous Media, 2nd ed., Springer, New York, 1995.
12. P.-H. Gao et al. Microstructure and Properties of Densified Gd_2O_3 Bulk. *Materials* **2022**, *15*, 7793.
13. S. Balabanov et al. Thermal Conductivity of Yttria-Gadolinia Solid Solution Optical Ceramics in the Temperature Range 50–300 K. *Inorganics* **2022**, *10*, 78.
14. Q. Mistarihi, F. B. Sweidan, H. J. Ryu, Thermo-physical properties of bulk Gd_2O_3 for fuel performance analysis of a lumped burnable absorber fuel design, Transactions of the Korean Nuclear Society Autumn Meeting, Gyeongju, Korea, October 26-27, 2017.
15. S. Redmond, S. C. Rand, X. L. Ruan, M. Kaviany. Multiple scattering and nonlinear thermal emission of Yb^{3+}, Er^{3+}:Y_2O_3 nanopowders. *J. Appl. Phys.*, **2004**, *95*, 4069-4077.
16. L. Wang et al. Computer simulation of the packing of nanoparticles. *Powder Technol.* **2022**, *401*, 117317.

17. H. Wu, S. Grabarnik, A. Emadi, G. de Graaf, R. F. Wolffenbuttel. Characterization of thermal cross-talk in a MEMS-based thermopile detector array. *J. Micromech. Microeng.* **2009**, *19*, 074022.